Principles of Dynamic Heterogeneous Catalysis: Surface Resonance and Turnover Frequency Response

M. Alexander Ardagh,[†,‡] Omar A. Abdelrahman,[‡,§] and Paul J. Dauenhauer[*,†,‡]

†Department of Chemical Engineering and Materials Science, University of Minnesota, 421 Washington Ave SE, Minneapolis, Minnesota 55455, United States

‡Catalysis Center for Energy Innovation, University of Delaware, 221 Academy Street, Newark, Delaware 19716, United States

§Department of Chemical Engineering, University of Massachusetts Amherst, 159 Goessmann Laboratory, 686 North Pleasant Street, Amherst, Massachusetts 01003, United States

Ⓢ *Supporting Information*

ABSTRACT: Acceleration of the catalytic transformation of molecules via heterogeneous materials occurs through design of active binding sites to optimally balance the requirements of all steps in a catalytic cycle. In accordance with the Sabatier principle, the characteristics of a single binding site are balanced between at least two transient phenomena, leading to maximum possible catalytic activity at a single, static condition (i.e., a "volcano curve" peak). In this work, a dynamic heterogeneous catalyst oscillating between two electronic states was evaluated via simulation, predicting catalytic activity as much as three-to-four orders of magnitude (1000−10 000) above the Sabatier maximum. Surface substrate binding energies were varied by a given amplitude ($0.1 < \Delta U < 3.0$ eV) over a broad range of frequencies ($10^{-4} < f < 10^{11}$ s^{-1}) in square, sinusoidal, sawtooth, and triangular waveforms to characterize surface dynamics impact on average catalytic turnover frequency. Catalytic systems were shown to exhibit order-of-magnitude dynamic rate enhancement at "surface resonance" defined as the band of frequencies (e.g., 10^3−10^7 s^{-1}) where the applied surface waveform kinetics were comparable to kinetics of individual microkinetic chemical reaction steps. Key dynamic performance parameters are discussed regarding industrial catalytic chemistries and implementation in physical dynamic systems operating above kilohertz frequencies.

KEYWORDS: *catalysis, sabatier, dynamics, frequency, resonance, volcano*

THE GREAT WAVE OVER SABATIER VOLCANO
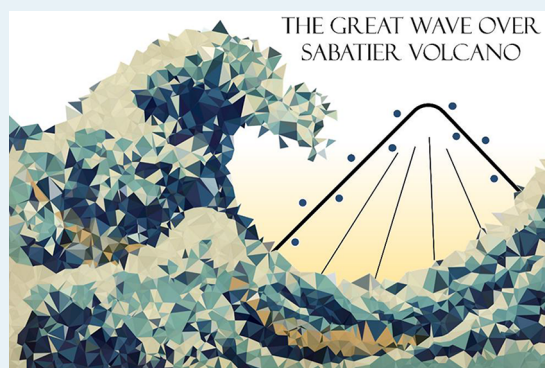
INTRODUCTION

Heterogeneous catalysis is an integral component of many industrial processes that manufacture food, materials, and energy for a high quality of life.[1] Catalytic surfaces, pores, and single-atom sites are responsible for accelerating the rates of reactions that protect and provide the most important resources including fuels,[2] fertilizers,[3] medicines,[4] basic chemicals,[5,6] CO_2 feedstock,[7] clean air,[8] and polymers[9,10] that would be inaccessible absent catalytic acceleration. In the past century, enhancement of these processes has progressed via increased catalyst selectivity and stability along with increased overall activity for smaller reactors that operate at higher efficiency and lower temperature.[11]

Catalytic rate enhancement occurs primarily through catalyst design to tune the binding characteristics of surface species and transition states for maximum catalytic turnover frequency.[12−14] In the past two decades, advances in nanostructured materials led to detailed synthesis of atomic-scale active sites that precisely balance the surface substrate binding energies.[15] The limit of this approach is characterized by the Sabatier principle, which states that the binding of substrates must be neither too strong nor too weak.[16,17] Quantitative description of the Sabatier principle was captured in Balandin-Sabatier volcano-shaped curves ("volcano curves" for the remainder of the manuscript), which depicted a metric of catalyst activity relative to a descriptor of substrate binding.[18,19] Balandin depicted volcano-shaped curves in 1960 and 1964 for the dehydration and dehydrogenation of alcohols, with the catalytic activity dependent on the bond energies between the alcohol oxygen and the metal oxide catalysts.[18,19] Since that time, volcano curves have been generated for numerous catalytic chemistries including NO_x decomposition,[20] propylene oxidation,[21] hydrodesulfurization,[22,23] ammonia synthesis,[24,25] CO oxidation,[26] and oxygenate decomposition,[27] among many other reactions.[28]

The simplest surface catalytic mechanism of species A reacting to species B depicted in Figure 1A obeys the Sabatier principle regarding adsorption enthalpy (ΔH_A ΔH_B) and surface reaction activation energy, (E_a). Reactant molecule A adsorbs to
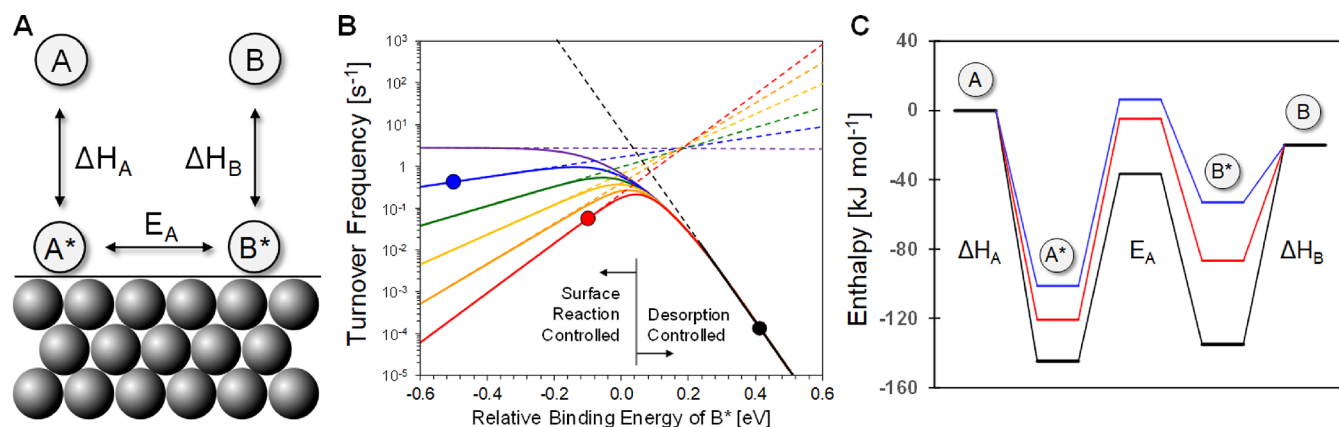
Figure 1. Catalyst Optimization via the Sabatier Principle. A. Surface reaction of A converting to B via transition state with forward activation energy, E_A. B. Volcano plots for the turnover frequency of A-to-B with variable binding energy of A* and B* and variable Brønsted–Evans–Polanyi relationships of E_a to ΔH_{sr} ($0 \leq \alpha \leq 1.0$:0.2 increments, purple to red). Conditions: perfectly mixed reactor at 150 °C, $Y_B \approx 1\%$. C. Three conditions of surface intermediate binding energy: black (+0.4 eV), red (−0.1 eV, $\alpha = 1.0$), and blue (−0.5 eV, $\alpha = 0.2$).
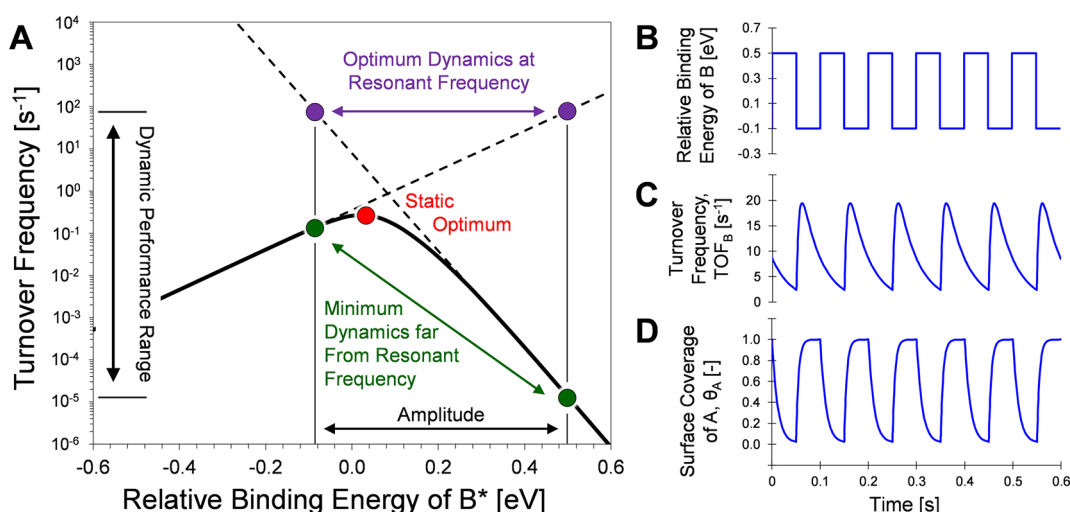

Figure 2. Dynamic Catalysis − Conditions and Surface Response. A. Transient variation of the catalyst surface ($\alpha = 0.8$) binding between a maximum and minimum binding energy comprises the overall surface amplitude resulting in dynamic performance with optimum (purple) turnover frequency at the reaction resonance frequency. B−D. (B) The catalyst binding energy changes as a square wave below the resonant frequency ($f = 10$ Hz), (D) resulting in maximum and minimum surface coverage of surface intermediates B* and A*; (C) loading and unloading of B from the surface produces transient B production rates.

the surface as A*, undergoes surface reaction to B*, and then desorbs to gas-phase product B; the overall turnover rate can potentially be limited by any one of these three steps. Reactant adsorption is a fast, barrierless step unless it is combined with surface reactions; a combined step of dissociative adsorption (e.g., N$_2$) is commonly rate limiting on some catalytic materials.[29] The volcano curve therefore results from the sequential kinetics of surface reaction(s) and product desorption, as presented originally by Balandin and depicted in Figure 1B, the transition between surface reaction- and desorption-control exhibits the characteristic "volcano" two-kinetic-regime plot. As depicted in Figure 1C, surface adsorbates desorb slowly on strong-binding materials, while surface reactions occur slowly on weak-binding materials; the kinetic balance of these two steps forms the optimum turnover frequency of the system (i.e., volcano peak) characteristic to materials only exhibiting the optimal binding energy.[30]

The asymmetry of some volcano curves depicted in Figure 1B arise from the relationship between the surface binding energy and the surface reaction activation energy. As described in the

Brønsted−Evans−Polanyi (BEP) principle,[31,32] the activation energy of a catalytic reaction linearly correlates with the surface reaction enthalpy by a linear-scaling parameter, α, and offset of E_0 associated with a reaction class.[33]

BEP relationship:

$$E_a = \alpha^* \Delta H_{sr} + E_0 \qquad (1)$$

As depicted in Figure 1B, $\alpha \approx 0$ (purple) indicates negligible relationship between the enthalpy of surface reaction and the surface activation energy resulting in a "flat" volcano, while a completely proportional relationship, $\alpha \approx 1.0$ (red), forms a more symmetric volcano curve; values between zero and one form the interspersed curves: blue of $\alpha \approx 0.8$, green of $\alpha \approx 0.6$, yellow of $\alpha \approx 0.4$, and orange of $\alpha \approx 0.2$ all with an offset E_0 of 102 kJ/mol. The linear scaling relationships can be universal and consistent across different molecules,[34−37] while other chemicals such as formic acid exhibit different linear scaling relationships across different transition metal groups of the periodic table.[38] The set of volcano curves in Figure 1B are also defined by the condition that the surface energy of B* changes at

twice the rate of the surface energy of A*, which is a ratio that can vary between surface chemistries and materials.

Catalyst activity optimization within the context of volcano curves has focused on catalyst design to achieve optimal turnover at the volcano curve apex. Of the existing catalysts and multimetal combinations, computational screening of the relevant surface-binding descriptors aims to identify single- or multidescriptor optima from databases of catalytic materials.[39−41] Other strategies have aimed to create and tune the properties of new materials including physical and electronic descriptors such as metal spacing and coordination, d-band center and Fermi level, and electronic interaction with supports, solvents, and coadsorbents via multimetal mixing and/or nanostructured synthesis;[42−47] all of these approaches have achieved success in creating new materials near the maximum theoretical turnover frequency of a static catalyst.

The limitation of the Balandin-Sabatier maximum arises from the multipurpose catalyst, which must balance the kinetics of competing reaction steps (activation, desorption, etc.). One strategy to exceed this maximum is to decouple the reaction phenomena and physically disassociate sequential chemistries. The physical reaction dissociation approach was recently demonstrated with ammonia synthesis, whereby gas-phase activation of N_2 occurred via plasma, and metals catalyzed hydrogenation of nitrogen to ammonia with rapid desorption.[48,49] Deconvoluted control of individual reactions (activation with plasma and hydrogenation with a metal catalyst) permits independent system tuning to yield an overall rate potentially in excess of the Balandin−Sabatier maximum in conventional catalytic reactors.

We will focus on the simulated kinetics of temporally decoupling surface reaction steps via an oscillation of the catalytic surface binding energy. As depicted in Figure 2A, the volcano curve can be depicted with its independent slopes extended above the apex (dashed black lines); these represent the potential rates of surface reaction and desorption absent other limitations. In a dynamic system, the surface energy could oscillate between two or more binding energy states, with the oscillation amplitude identified as the total distance in traversed binding energy (ΔU [=] eV) at the frequency of oscillation (f [=] s^{-1}); in Figure 2A, the volcano plot has a BEP of moderate slope, $\alpha \approx 0.8$, and amplitude (-0.10 to $+0.50$ eV, $\Delta U = 0.60$ eV). The optimal turnover frequencies are depicted for each state at the given amplitude as purple points, while the minimum turnover frequencies below the static optimum are identified as green points.

The response of the substrate on the catalyst surface depends on the relative dynamics of the system to the kinetics of the surface steps (i.e., reactions and desorption). For a catalyst oscillating between two states as a square waveform with amplitude of ΔU and frequency ($f \approx \tau^{-1}$), the optimum time-averaged turnover frequency will occur when the time scale of each state is approximately the same as the time scale of the individual surface steps. Referred to here as "surface resonance", the resonant frequencies depicted in Figure 2A permit the surface coverage of B* to vary ($\theta_{min} < \theta_B < \theta_{max}$) without stabilization before switching surface states.

Several physical methods exist to modulate the surface binding energy of substrates on catalyst surfaces via external stimulus. The application of strain to a metal surface alters its electronic structure, thereby influencing the binding energies of adsorbed molecules.[50−53] Additionally, applied external fields interact with a surface chemisorption bond and alter the

adsorbate binding energy; field strength in excess of 0.1 V/Å has been shown to alter adsorbate molecular orbitals and therefore adsorbate binding energy.[54−56] Intrinsic electric fields, such as those present in electrochemical systems, can also shift the binding energy of absorbates on the surface of an electrode. Alternative methods include back-gated electrodes, which have tunable electronic structure and electrochemical kinetics due to the presence of charge carriers generated on a metal or metal oxide surface.[57,58] However, the impact on the overall rate of catalytic reaction remains to be determined for external stimulus (e.g., strain or electric field) applied statically or dynamically to catalyst surface intermediates (i.e., binding energy) and transition states.

In this work, oscillatory binding energy is evaluated for its impact on the kinetics of heterogeneous catalysis to understand the requirements for external stimuli such as strain or electric fields. The concept of "dynamic catalysis" illustrated in Figure 2A is explored via simulation for a broad range of catalyst and dynamic applied conditions to understand the connection between catalyst-system design combinations and catalytic turnover frequency. For BEP relations identified in Figure 1B ($0 \leq \alpha \leq 1.0$), we present the averaged turnover frequency for a broad range of conditions including applied frequency (f), surface energy amplitude (ΔU), and wave shape (e.g., square versus sinusoidal). Optimal performance is then identified with the constraints of practical implementation in mind.

■ RESULTS AND DISCUSSION

The following results were generated computationally using Matlab (see the Methods section for more details). Turnover frequencies (TOFs) were calculated at 1% yield of product (B) in all cases for a CSTR reactor setup. TOF$_B$ can be defined as follows:

$$\text{TOF}_B = [B]\frac{\dot{q}}{\text{\# of active sites}}[\,=\,]\text{s}^{-1} \tag{2}$$

where $\dot{q}$ is the volumetric flow rate through the reactor and $[B]$ is the concentration of component B in the reactor effluent.

The impact of oscillating the surface binding energy of B* with time is depicted in Figure 2B−D for a square waveform of amplitude $\Delta U \approx 0.6$ eV and frequency of $f \approx 10$ Hz. The square waveform of surface binding energies of B* depicted in Figure 2B was simulated for a perfectly mixed reactor operating at 1% yield of B, 150 °C, and 100 bar A inlet. These conditions produce the instantaneous turnover frequency depicted in Figure 2C which ranges from 3 to 19 s^{-1} in a complex oscillating form; the TOF$_B$ achieves a maximum of 19 s^{-1} soon after the binding energy of B* switches to relatively low energy (BE$_B \approx$ 0.9 eV), while the minimum TOF$_B$ of 3 s^{-1} occurs just before BE$_B$ switches from 1.5 to 0.9 eV. These turnover frequencies of B are below the predicted resonance frequencies identified in purple in Figure 2A ($\sim$100 s^{-1}). An explanation for the lower-than-expected TOF$_B$ is provided by the surface coverages of Figure 2D. At 10 Hz, the surface coverage of A* achieves complete oscillation between $\theta_A \approx 0$ and 1; moreover, the surface coverage of A* stabilizes for a significant fraction of the period of oscillation, indicating a period ($\sim$0.02 s) with negligible change in the surface composition of the catalyst. In other words, faster oscillation above 10 Hz of the surface binding energy of B* should more efficiently utilize the catalyst.

The TOF$_B$ of Figure 2C indicate that the highest rates occur when surface states flip from high to low binding energy of B*. The energetic path leading to this unloading of the surface of B*
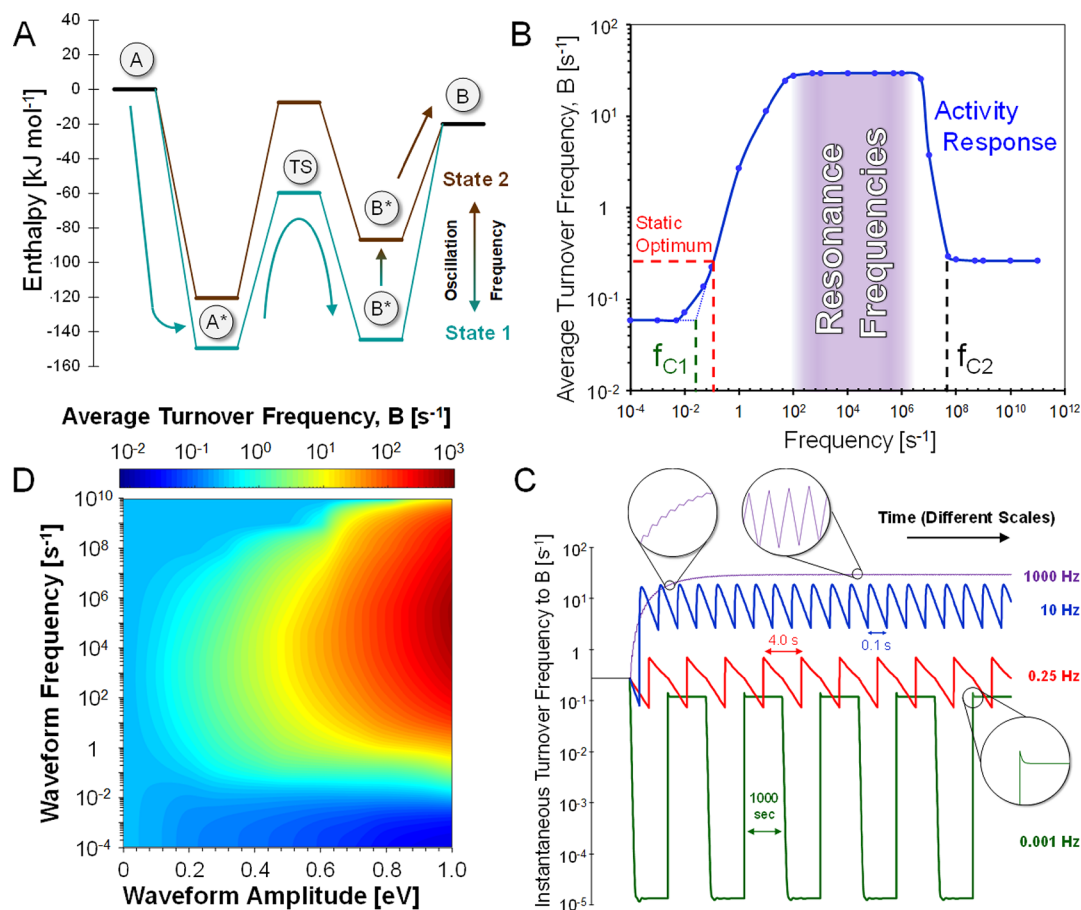
Figure 3. Activity response of applied oscillating surface binding energy - square waveform. A. Oscillating state energy diagram for A reacting on a catalytic surface to B product (−0.1 to 0.5 eV of B*). B. Average catalytic turnover frequency to product B at waveform amplitude of 0.6 eV at 150 °C and 100 bar; resonance frequencies identified in purple. C. Instantaneous turnover frequency to B for four frequencies at ΔU of 0.6 eV at 150 °C and 100 bar. D. Average turnover frequency to B at 150 °C and 100 bar for variable square waveform amplitude and frequency.

is depicted in Figure 3A. In the initial strong binding state 1, A adsorbs to the surface as A* and forms a thermodynamic distribution with state B*. When the surface flips to weaker-binding state 2, B* readily desorbs with lower activation energy to form product B. By these two states, the complete cycle can be interpreted as filling of the surface sites (state 1) followed by forced desorption (state 2), the overall rate of which is determined by the surface frequency and amplitude associated with the surface binding energies of the two states.

The impact of the surface state-flipping frequency on the time-averaged turnover frequency is depicted in Figure 3B for fixed square waveform amplitude ($\Delta U = 0.6$ eV). At low frequencies ($10^{-4} < f < 10^{-2}$ Hz), the average TOF_B is an average of the static conditions of the two states (i.e., a slow catalyst). At the corner frequency (f_{C1}) of ~0.02 Hz, the average turnover frequency begins to increase until the dynamic system eventually matches the optimal turnover frequency of the static system at the volcano apex (depicted in red). Further increasing the surface waveform frequency increases the average turnover frequency until maximizing over a range of dynamic resonance ($\sim 10^3 < f < \sim 10^7$), identified in Figure 3B in purple. Above the resonance frequency band, the average turnover frequency decreases before stabilizing at 10^{-1} s^{-1} at a waveform frequency of ~10^{11} Hz, the TOF_B associated with optimal conditions of the static system at the volcano curve optimum.

For the volcano curve system depicted in Figure 2A with amplitude of 0.6 eV square waveform, the instantaneous TOF_B is

depicted in Figure 3C for four frequencies: 0.001 Hz in green, 0.25 Hz in red, 10 Hz in blue, and 1000 Hz in purple. At low frequency (0.001 Hz), the surface coverages of A* and B* (in the Supporting Information (SI), Figure S2) rapidly respond to the change in surface state, with static operation occurring in either of the two states. Low frequency below f_{C1} results in TOF_B response comparable to a mix of the two low activity states identified in green in Figure 2A. The unique behavior to the general TOF_B response exists only at the condition of flipping surface states from strong to weak binding of B*; as noted in the highlighted region of Figure 3C for 0.001 Hz, the TOF_B overshoots, resulting from the unloading of surface B* species into the gas phase as product B. As the waveform frequency increases to 0.25 and 10 Hz, the unloading of B* species from the surface becomes the dominant mechanism leading to catalyst activity. For these two frequencies, the TOF_B and the surface coverages of A* and B* (Figure S3−S4) are transient for most of the waveform period. At 1000 Hz in Figure 3C, the TOF_B and surface coverages of A* and B* (Figure S5) are always transient; under these conditions TOF_B and surface coverages only minimally oscillate in value (e.g., $0.29 < \theta_B < 0.32$).

An interpretation of catalytic surface resonance comes from evaluating the TOF_B response of each condition independently, as shown in Figure 3C. The rate of production for surface species B* is defined by the forward surface reaction rate constant and surface coverage of A* (which is in equilibrium with gas phase
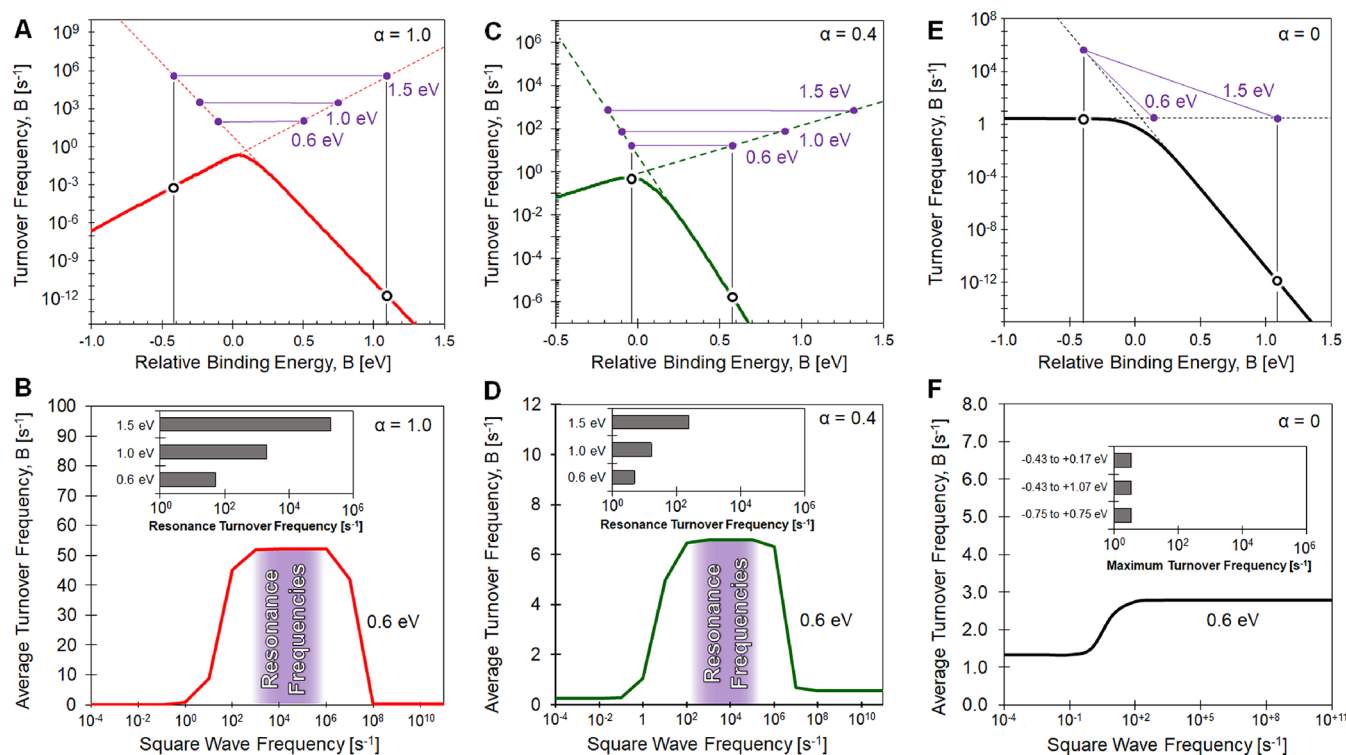
Figure 4. Dynamic catalytic response of three linear-scaling relationships (α of 1.0, 0.4, and 0.0). All panels comprised of an A-to-B reaction at 150 °C, 100 bar, perfectly mixed system operating at 1% yield of product B with BEP relationship parameter α as the sole variable. A. Volcano plot for α of 1.0 system. B. Catalytic turnover frequency response of α of 1.0 system. C. Volcano plot for the α of 0.4 system. D. Catalytic turnover frequency response of the α of 0.4 system. E. Volcano plot for the α of zero system. F. Catalytic turnover frequency response of the α of zero system.

A). Similarly, the rate of desorbing B* to gas product B is defined by the desorption rate constant and surface coverage of B*. In this case, the time scales of these two processes sum to the total time scale, which is comparable to the applied square waveform time scale at resonance. This concept is visually observed in Figure 2A, where TOF_B for the two purple points predict 60 s^{-1} for each independent process, while the actual TOF_B predicted by simulation is exactly half of that value, 29 s^{-1} (Figure 3B and 3C). To put it simply, catalytic surface resonance occurs when the frequency of the applied surface state-switching waveform matches the natural frequency of the catalytic kinetics.

Variation of the surface square waveform amplitude will change the kinetics of the surface chemistry, resulting in a shift of the resonance frequency band. As depicted in the heat map of Figure 3D, a range of amplitudes $(0 < \Delta U < 1.0$ eV$)$ was evaluated for the volcano curve of Figure 2A for frequencies varying over 14 orders of magnitude $(10^{-4} \leq f \leq 10^{10}$ s$^{-1})$ to determine the average steady state turnover frequency to B, TOF_B. The steady state system response is oscillatory, so the average TOF was calculated via integration over a range of time after the system reached stable oscillation. For each value of the oscillation amplitude ΔU, the two extreme values of U [eV] corresponding to the two states of the square surface waveform were selected to yield two conditions of equal rate; put simply, each value of ΔU should produce a horizontal line connecting two purple points as in Figure 2A. The variation in surface kinetics with square waveform frequency and amplitude is visually apparent in Figure 3D, where low frequencies below 0.1 Hz are slower (dark blue) than static catalysis for amplitudes greater than 0.1 eV. Alternatively, above ~1 Hz, the average turnover frequency increases dramatically to 10 and 1000 s^{-1} per catalytic site for amplitudes above 0.3 eV.

The ability to dynamically accelerate catalytic turnover depends on the energetics of the obtainable states defined by the shape of the volcano curve. Of the many parameters that define the volcano shape, the linear-scaling relationship parameter, α, relating the surface reaction enthalpy to the surface reaction activation energy can dramatically shift the slope of the volcano plot. While Figures 2 and 3 describe a system with α of 0.8, three volcano plots for α of 1.0, 0.4, and 0 are shown in Figure 4. For steep volcano plots such as Figure 4A, extension of the slopes as dashed lines above the volcano apex indicate rapid increase in the turnover frequency for amplitudes of 0.6, 1.0, and 1.5 eV at resonance conditions. This is supported by the catalytic reactor simulation kinetics of Figure 4B, which considered the catalyst system of Figure 4A at variable applied square waveform frequency $(10^{-4} < f < 10^{11})$. For a square waveform at an amplitude of 0.6 eV, the resonance frequencies of 10^3 to 10^7 s^{-1} yield an average turnover frequency to B of about 52 s^{-1} per catalytic site. At higher amplitudes of 1.0 and 1.5 eV, the average turnover frequency per catalytic site at resonance achieves 2,074 and 2.0×10^5 s^{-1}.

A broader volcano of α of 0.4 in Figure 4C limits the overall speed achievable for a given amplitude; the purple points above the curve are further apart and at lower turnover frequencies. This translates to lower overall reaction rates at resonance conditions as shown in Figure 4D. At the extreme case where the activation energy of the surface reaction does not change with the binding energy of an adsorbate such as the volcano curve of Figure 4E, the potential of dynamic operation is limited as shown in Figure 4F. There exist at least two cases where the slope of the volcano curve is horizontal on one side as drawn: (1) catalytic systems where the surface reaction enthalpy does not change with the binding energies of the descriptor component
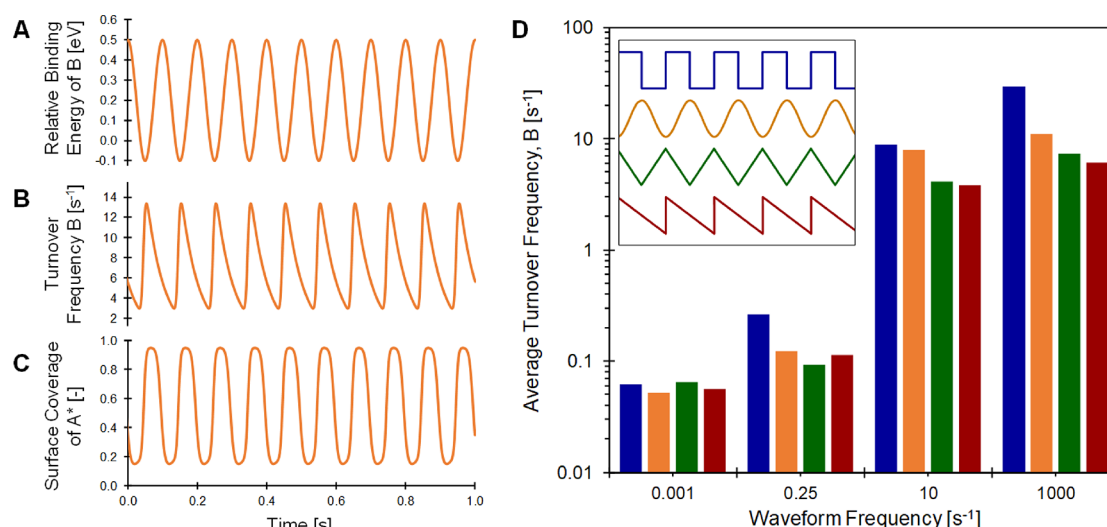
Figure 5. Surface B* Binding Energy Waveform. Volcano curves comprised of $\Delta U \sim 0.6$ eV, 150 °C, perfectly mixed reactor at 1% yield of B product. A. Relative binding energy of B* varying in sinusoidal waveform at $f \approx 10$ Hz. B. Turnover frequency to B response to a 10 Hz sinusoidal waveform. C. Surface coverage of A* response to a 10 Hz sinusoidal waveform. D. Comparison of average turnover frequency to B for an applied B* surface binding energy oscillation of four waveform types: square (blue), sinusoidal (orange), triangle (green), and sawtooth (red).

(e.g., B*), thus leading to constant surface activation energy of reaction, and (2) systems with α of zero. In these rare cases, the rate of the surface reaction can never be accelerated to match a fast rate of desorption, and the average overall turnover frequency is limited to the rate of the surface reaction.

Applying dynamic operation to heterogeneous catalytic applications will require identifying the conditions of optimal performance in addition to new design variables such as surface waveform shape that can be implemented in real reactor technology. As depicted in Figure 5A, the sinusoidal surface binding waveform varying from −0.1 to +0.5 eV at frequency of 10 Hz applied to the catalyst system characterized by the volcano plot of Figure 2A yields oscillatory turnover frequency (Figure 5B) and surface coverage of A* (Figure 5C) at 100 bar A inlet, 150 °C, and 1% yield of B. Similar to the case with the square waveform, the turnover frequency of B increases when the applied waveform changes from strong binding of B* to weak binding. At the same time the surface coverage of A* increases to take the place of the B* that was removed from the surface as desorbed product B. Other considered waveform types including triangle and sawtooth are depicted in Figure 5D. For all conditions, the square waveform exhibits superior activity at surface resonance conditions. At higher frequencies of 10 and 1,000 Hz, the sinusoidal waveform outperforms the triangle and sawtooth shapes.

Implementation of dynamic operation of heterogeneous catalysts requires the capability to modify the binding energy of surface intermediates with time. Based on the simulations of Figures 2−5, catalyst and system parameters should be selected to achieve average turnover frequencies above the optimum of static conditions and preferably as high as resonance conditions. This implies that a physical catalyst system must achieve surface waveform amplitudes of at least 0.3 eV (and preferably above 0.5 eV) and operating frequencies above 10 Hz (and preferably 100−1000 Hz), which is a significant challenge for experimental implementation. These performance targets change with the selected surface chemistry, which will likely have more than two surface intermediates exhibiting linear scaling relationships over a broad range ($0.2 < \alpha < 0.8$). The complexity of each catalytic chemistry combined with the large number of dynamic catalysis parameters indicates that each system can be guided by the principles proposed here but will require detailed microkinetic modeling for design and optimization.

Device construction for tuning of the surface intermediate adsorbate binding energy can be interpreted via the electronic state of the catalyst material; surface intermediates such as adsorbed nitrogen, N*, correlate linearly with the d-band edge/center when compared across a broad range of metals.[17,59−61] Temporal variation of metal d-bands exists in at least two categories including electronic and physical (and even electro-mechanical) manipulation. As stated earlier, straining of surfaces has been shown to shift the d-band centers of metals, metal alloys, and other 2D materials,[62] which alters the binding energy of adsorbates such as carbon monoxide.[63] When combined with dynamic approaches such as sound waves or piezoelectrics capable of 1% strain oscillation exceeding kilohertz frequencies, this approach can potentially achieve the frequencies and amplitudes required for resonant dynamic catalytic acceleration. Other methods electronically manipulate a catalyst surface including field effect modulation[57,58,64] or non-Faradaic electro-chemical modification,[65−69] both of which can potentially achieve the frequency (>100 Hz) and amplitude targets necessary for surface catalytic resonance. Future work will expand the principles developed here to more complex surface chemistries in parallel with implementation in physical catalytic reactors.

■ METHODS

Continuously stirred tank reactor (CSTR − perfect mixing assumed) models were implemented in Matlab 2017b and Matlab 2018b, using GPU computing resources at the Minnesota Supercomputing Institute (MSI) at the University of Minnesota. See the SI section S1 for the full shell and reactor codes, which can be used and modified to reproduce these simulations. The shell code set reactor parameters included the temperature (T), inlet volumetric flow rate ($\dot{q}$), catalyst weight (w), and active site loading. Reactor time-on-stream data was generated using the Matlab ODE15s differential equation solver. This solver was selected based on its performance; see the SI

section S2 for a comparison with Matlab ODE45, ODE23s, ODE23t, and ODE23tb. The set of differential equations consisted of forward and reverse rates for the consumption of gas phase (A, B) and surface species (A*, B*). This general reaction system, A ↔ B, was modeled using three reversible elementary steps: (i) adsorption of A, (ii) conversion of A* to B*, and (iii) desorption of B with a site balance involving *, A*, and B*.

$$A \rightleftharpoons A^* \tag{3}$$

$$A^* \rightleftharpoons B^* \tag{4}$$

$$B^* \rightleftharpoons B \tag{5}$$

$$[sites] = [*] + [A]^* + [B]^* \tag{6}$$

Generalized forms of the differential equation used for each gas phase and surface species are

$$\frac{d[A]}{dt} = \frac{\dot{q}}{V}([A]_{feed} - [A]) - r_{1,forward} + r_{1,reverse} \tag{7}$$

$$\frac{d[A]^*}{dt} = r_{1,forward} - r_{1,reverse} - r_{2,forward} + r_{2,reverse} \tag{8}$$

Reaction rate equations consisted of rate constants and species concentrations, with each elementary step assumed to be first order in all participating reactants. Since this was modeled as a gas phase reaction, adsorption steps were expressed in terms of A and B pressures (bar).

$$r_{ads,i} = k_{ads,i} P_i [*] \tag{9}$$

$$r_{des,i} = k_{des,i} \theta_i [sites] \tag{10}$$

$$r_{surfrxn,forward} = k_{surfrxn,forward} * \theta_A [sites] \tag{11}$$

Rate constants were constructed as Arrhenius expressions using pre-exponential factors and activation energies for adsorption, desorption, and surface reactions.[70] Pre-exponential factors were set to 10^6 (bar s)$^{-1}$ for adsorption steps and 10^{13} s^{-1} for surface reaction and desorption steps. These values are typical starting points when fitting microkinetic models to experimental data. Activation energy was set to 0 kJ/mol for adsorption and to the binding energies (BEs) of A and B for their respective desorption steps. The binding energies for A and B, the surface reaction activation energy (E_a) and the surface enthalpy of reaction were selected; the base conditions were BE_A = 1.3 eV, BE_B = 1.0 eV, E_a = 102 kJ mol^{-1}, ΔH_{sr} = 0 kJ/mol, and ΔH_{ovr} = −20 kJ/mol.

Brønsted−Evans−Polanyi relationships between E_a and BEs were held at a constant offset (E_0) of 102 kJ/mol and the slope of the relationship, α, was varied ($0 \leq \alpha \leq 1.0$). These values fall within previously observed ranges for experimentally derived BEP parameters and resulted in volcano peak TOFs between 0.1 and 10 s^{-1}. Thus, the activation energy was expressed as a linear function of the surface enthalpy of reaction, ΔH_{sr} (i.e., the difference in binding energies between A* and B* plus the overall enthalpy of reaction from A → B):

$$E_a = \alpha * \Delta H_{sr} + E_0 \tag{12}$$

Volcano plots were generated by varying ΔH_{sr} and measuring the time-averaged turnover frequency (TOF) at 1.0% overall yield of B. Turnover frequency was defined as $TOF = [B]\frac{\dot{q}}{\text{\# of sites}}$ for the CSTR design equation, so in practice $\dot{q}$ (the gas flow rate [=] L/s) was adjusted until the outlet yield of component B was 1.0%. Variation in the BEP slope ($0 \leq \alpha \leq 1.0$) resulted in

surface reaction activation energies ($25 < E_a < 170$ kJ/mol) between binding energies of 0.5 and 2.0 eV, which are comparable with a broad range of reactions described in the literature.

Dynamic catalysis was simulated by running ODE15s for a system where BEs varied with time on stream as square, sinusoidal, triangle, or sawtooth waves. Binding energy changes for A* and B* were specified in the shell code, and these shifts resulted in varying ΔH_{sr} and E_a. Oscillation period/frequency was set by specifying the time duration spent at each condition. Reported TOFs were calculated when the system oscillation was centered on 1.0% yield of B and after the reactor had achieved oscillatory steady state, defined as a steady time-averaged turnover frequency. Example time on stream data for dynamic catalysis can be found in the SI section S4.

Plots of the average turnover frequency as a function of surface binding energy oscillation amplitude and frequency (i.e., heat maps) were generated in Matlab 2018b using the jet color scheme to indicate low and high TOF, ranging from dark blue to dark red. The heat map data consists of a modified Akima cubic Hermite fit through discrete data points calculated at 0−1.0 eV ΔBE. Data points are tabulated in the SI section S5. This data was obtained for symmetric dynamic catalysis starting at the volcano peak ($\Delta BE \approx -0.05$ to $+0.05$ eV) and oscillating the same amplitude in each direction (from 0 to 0.75 eV). Data was also obtained for asymmetric dynamic catalysis where the end points were chosen based on extrapolated linear fits of each side of the volcano curve. These lines were set equal with a specified oscillation amplitude between 0 and 1.5 eV, and the end points were chosen by drawing a vertical line down to the volcano plot. Frequency response figures were generated for scenarios with varying BEP relationships where the BEP slope ranged from zero to one.

■ ASSOCIATED CONTENT

Ⓢ Supporting Information

The Supporting Information is available free of charge on the ACS Publications website at DOI: 10.1021/acscatal.9b01606.

> Matlab 2017b and 2018b volcano plot generation code; square, triangle, and sawtooth waveform dynamic catalysis code; sinusoidal waveform dynamic catalysis code; static catalysis data from the CSTR model; time on stream data for oscillation frequencies of 0.001−1000 Hz with a square waveform; time on stream data for an oscillation frequency of 10 Hz with a square, triangle, sawtooth, or sinusoidal waveform. (PDF)

■ AUTHOR INFORMATION

Corresponding Author
*E-mail: hauer@umn.edu.
ORCID ⦿
M. Alexander Ardagh: 0000-0002-0636-8215
Paul J. Dauenhauer: 0000-0001-5810-1953

Notes
The authors declare no competing financial interest.

■ ACKNOWLEDGMENTS

■ REFERENCES

(1) Catlow, C. R.; Davidson, M.; Hardacre, C.; Hutchings, G. J. Catalysis is Making the World a Better Place. *Philos. Trans. R. Soc., A* **2016**, *374*, 1−2.

(2) Narsimhan, K.; Iyoki, K.; Dinh, K.; Roman-Leshkov, Y. Catalytic Oxidation of Methane into Methanol over Copper-Exchanged Zeolites with Oxygen at Low Temperature. *ACS Cent. Sci.* **2016**, *2*, 424−429.

(3) Medford, A. J.; Wellendorff, J.; Vojvodic, A.; Studt, F.; Abild-Pedersen, F.; Jacobsen, K. W.; Bligaard, T.; Norskov, J. K. Assessing the Reliability of Calculated Catalytic Ammonia Synthesis Rates. *Science* **2014**, *345*, 197−200.

(4) Busacca, C. A.; Fandrick, D. R.; Song, J. J.; Senanayake, C. H. The Growing Impact of Catalysis in the Pharmaceutical Industry. *Adv. Synth. Catal.* **2011**, *353*, 1825−1864.

(5) Arora, S. S.; Nieskens, D. L. S.; Malek, A.; Bhan, A. Lifetime Improvement in Methanol-to-Olefins Catalysis over Chabazite Materials by High-Pressure H₂ Co-Feeds. *Nature Catalysis* **2018**, *1*, 666−672.

(6) Patet, R. E.; Nikbin, N.; Williams, C. L.; Green, S. K.; Chang, C. C.; Fan, W.; Caratzoulas, S.; Dauenhauer, P. J.; Vlachos, D. G. Kinetic Regime Change in the Tandem Dehydrative Aromatization of Furan Diels-Alder Products. *ACS Catal.* **2015**, *5*, 2367−2375.

(7) Szuromi, P. *Science* **2016**, *354*, 429.

(8) Paolucci, C.; Khurana, I.; Parekh, A. A.; Li, S.; Shih, A. J.; Li, H.; Di Iorio, J. R.; Albarracin-Caballero, J. D.; Yezerets, A.; Miller, J. T.; Delgass, W. N.; Ribeiro, F. H.; Schneider, W. F.; Gounder, R. Dynamic Multinuclear Sites Formed by Mobilized Copper Ions in NOx Selective Catalytic Reduction. *Science* **2017**, *357*, 898−903.

(9) Hillmyer, M. A. The Promise of Plastics from Plants. *Science* **2017**, *358*, 868−870.

(10) Abdelrahman, O.; Park, D. S.; Vinter, K.; Spanjers, C.; Ren, L.; Cho, H. J.; Vlachos, D. G.; Fan, W.; Tsapatsis, M.; Dauenhauer, P. J. Biomass-Derived Butadiene by Dehydra-Decyclization of Tetrahydrofuran. *ACS Sustainable Chem. Eng.* **2017**, *5*, 3732−3736.

(11) U.S. Department of Energy *Basic Research Needs for Catalysis Science to Transform Energy Technologies: Report from the U.S. Department of Energy, Office of Basic Energy Sciences Workshop May 8−10, 2017*, in Gaithersburg, MD. Retreived Feb. 3, 2019. Link: https://science.energy.gov/~/media/bes/pdf/reports/2017/BRN_CatalysisScience_rpt.pdfhttps://science.energy.gov/~/media/bes/pdf/reports/2017/BRN_CatalysisScience_rpt.pdf.

(12) Chen, J. F.; Mao, Y.; Wang, H. F.; Hu, P. A Simple Method to Locate the Optimal Adsorption Energy for the Best Catalysts Directly. *ACS Catal.* **2019**, *9*, 2633−2638.

(13) Kari, J.; Olsen, J. P.; Jensen, K.; Badino, S. F.; Krogh, K. B. R. M.; Borch, K.; Westh, P. Sabatier Principle for Interfacial (Heterogeneous) Enzyme Catalysis. *ACS Catal.* **2018**, *8*, 11966−11972.

(14) Vojvodic, A.; Norskov, J. K. New Design Paradigm for Heterogeneous Catalysts. *National Science Review* **2015**, *2*, 140−149.

(15) Bell, A. T. The Impact of Nanoscience on Heterogeneous Catalysis. *Science* **2003**, *299*, 1688−1691.

(16) Sabatier, P. *La Catalyse en Chimie Organique, Librairie Polytechnique*, Paris et Liège, 1920.

(17) Medford, A. J.; Vojvodic, A.; Hummelshoj, J. S.; Voss, J.; Abild-Pedersen, F.; Studt, F.; Bligaard, T.; Nilsson, A.; Norskov, J. K. From the Sabatier Principle to a Predictive Theory of Transition-Metal Heterogeneous Catalysis. *J. Catal.* **2015**, *328*, 36−42.

(18) Balandin, A. A.; Ferapontov, V. A.; Tolstopyatova, A. A. The Activity of Cadmium Oxide as a Catalyst for Hydrogen Dehydrogenation. *Bull. Acad. Sci. USSR, Div. Chem. Sci.* **1960**, *9*, 1630−1636.

(19) Balandin, A. A. The Multiplet Theory of Catalysis. *Energy Factors in Catalysis* **1964**, *33*, 549−579.

(20) Vijh, A. K. Sabatier-Balandin Interpretation of the Catalytic Decomposition of Nitrous Oxide on Metal-Oxide Semiconductors. *J. Catal.* **1973**, *31*, 51−54.

(21) Vijh, A. Interpretation of Some Aspects of Catalytic Oxidation of Ammonia and Propylene by Semiconducting Oxides in Terms of Volcano-Shaped Plots. *J. Chim. Phys. Phys.-Chim. Biol.* **1973**, *70*, 1444−1447.

(22) Toulhoat, H.; Raybaud, P.; Kasztelan, S.; Kresse, G.; Hafner, J. Transition Metals to Sulfur Binding Energies Relationship to Catalytic Activities in HDS: Back to Sabatier with First Principle Calculations. *Catal. Today* **1999**, *50*, 629−636.

(23) Chianelli, R. R.; Berhault, G.; Raybaud, P.; Kasztelan, S.; Hafner, J.; Toulhoat, H. Periodic Trends in Hydrodesulfurization: in Support of the Sabatier Principle. *Appl. Catal., A* **2002**, *227*, 83−96.

(24) Ichikawa, S. Volcano-Shaped Curves in Heterogeneous Catalysis. *Chem. Eng. Sci.* **1990**, *45*, 529−535.

(25) Logadottir, A.; Rod, T. H.; Norskov, J. K.; Hammer, B.; Dahl, S.; Jacobsen, C. J. H. The Bronsted-Evans-Polanyi Relation and the Volcano Plot for Ammonia Synthesis over Transition Metal Catalysts. *J. Catal.* **2001**, *197*, 229−231.

(26) Vijh, A. Volcano Relationships in Catalytic Reactions on Oxides. *J. Catal.* **1974**, *33*, 385−391.

(27) Barteau, M. A. Linear Free Energy Relationships for C1-Oxygenate Decomposition on Transition Metal Surfaces. *Catal. Lett.* **1991**, *8*, 175−184.

(28) Medford, A. J.; Vojvodic, A.; Hummelshoj, J. S.; Voss, J.; Abild-Pedersen, F.; Studt, F.; Bligaard, T.; Nilsson, A.; Norskov, J. K. From the Sabatier Principle to a Predictive Theory of Transition-Metal Heterogeneous Catalysis. *J. Catal.* **2015**, *328*, 36−42.

(29) Munter, T. R.; Bligaard, T.; Christensen, C. H.; Norskov, J. K. BEP Relations for N₂ Dissociation over Stepped Transition Metal and Alloy Surfaces. *Phys. Chem. Chem. Phys.* **2008**, *10*, 5202−5206.

(30) Salciccioli, M.; Stamatakis, M.; Caratzoulas, S.; Vlachos, D. G. A Review of Multi-Scale Modeling of Metal-Catalyzed Reactions: Mechanism Development for Complexity and Emergent Behavior. *Chem. Eng. Sci.* **2011**, *66*, 4319−4355.

(31) Bell, R. P. The Theory of Reactions Involving Proton Transfers. *Proc. R. Soc. A* **1936**, *154*, 414.

(32) Evans, M. G.; Polanyi, M. J. Further Considerations on the Thermodynamics of Chemical Equilibria and Reaction Rates. *Trans. Faraday Soc.* **1936**, *32*, 1333.

(33) Sutton, J. E.; Vlachos, D. G. A Theoretical and Computational Analysis of Linear Free Energy Relations for the Estimation of Activation Energies. *ACS Catal.* **2012**, *2*, 1624−1634.

(34) Wang, S.; Petzold, V.; Tripkovic, V.; Kleis, J.; Howalt, J. G.; Skulason, E.; Fernandez, E. M.; Hvolbaek, B.; Jones, G.; Toftelund, A.; Falsig, H.; Bjorketun, M.; Studt, F.; Abild-Pedersoen, F.; Rossmeisl, J.; Norskov, J. K.; Bligaard, T. Universal Transition State Scaling Relations for (De)hydrogenation over Transition Metals. *Phys. Chem. Chem. Phys.* **2011**, *13*, 20760−20765.

(35) Wang, S.; Temel, B.; Shen, J.; Jones, G.; Grabow, L. C.; Studt, F.; Bligaard, T.; Abild-Pedersen, F.; Christensen, C. H.; Norskov, J. K. Universal Brønsted-Evans-Polanyi Relations for C-C, C-O, C-N, N-O, N-N, and O-O Dissociation Reactions. *Catal. Lett.* **2011**, *141*, 370−373.

(36) Vojvodic, A.; Calle-Vallejo, F.; Guo, W.; Wang, S.; Toftelund, A.; Studt, F.; Martinez, J. I.; Shen, J.; Man, I. C.; Rossmeisl, J.; Bligaard, T.; Norskov, J. K.; Abild-Pedersen, F. On the Behavior of Bronsted-Evans-Polanyi Relations for Transition Metal Oxides. *J. Chem. Phys.* **2011**, *134*, 244509.

(37) Loffreda, D.; Delbecq, F.; Vigne, F.; Sautet, P. Fast Prediction of Selectivity in Heterogeneous Catalysis from Extended Brønsted-Evans-Polanyi Relations: A Theoretical Insight. *Angew. Chem.* **2009**, *121*, 9140−9142.

(38) Barteau, M. A. Linear Free Energy Relationships for C1-Oxygenate Decomposition on Transition Metal Surfaces. *Catal. Lett.* **1991**, *8*, 175−184.

(39) Winther, K. T.; Hoffmann, M. J.; Mamun, O.; Boes, J. R.; Norskov, J. K.; Bajdich, M.; Bligaard, T., Catalysis-Hub.org: An Open

Electronic Structure Database for Surface Reactions. *Version 2. Chem. Rxiv. Preprint* DOI: 10.26434/chemrxiv.7336094.v2.

(40) Mpourmpakis, G.; Vlachos, D. G. Computational-Based Catalyst Design for Thermochemical Transformations. *MRS Bull.* **2011**, *36*, 211−215.

(41) Bo, C.; Maseras, F.; López, N. The Role of Computational Results Databases in Accelerating the Discovery of Catalysts. *Nature Catalysis* **2018**, *1*, 809−810.

(42) Hansgen, D. A.; Vlachos, D. G.; Chen, J. G. Using First Principles to Predict Bimetallic Catalysts for the Ammonia Decomposition Reaction. *Nat. Chem.* **2010**, *2*, 484−489.

(43) Williams, W. D.; Greeley, J. P.; Delgass, W. N.; Ribeiro, F. H. Water Activation and Carbon Monoxide Coverage Effects on Maximum Rates for Low Temperature Water-Gas Shift Catalysis. *J. Catal.* **2017**, *347*, 197−204.

(44) Herron, J. A.; Mavrikakis, M.; Maravelias, C. T. Optimization Methods for Catalyst Design. *Comput.-Aided Chem. Eng.* **2016**, *38*, 295−300.

(45) Gani, T. Z. H.; Kulik, H. J. Understanding and Breaking Scaling Relations in Single Site Catalysis: Methane to Methanol Conversion by FeIV = O. *ACS Catal.* **2018**, *8*, 975−986.

(46) Darby, M. T.; Stamatakis, M.; Michaelides, A.; Sykes, E. C. H. Lonely Atoms with Special Gifts: Breaking Linear Scaling Relationships in Heterogeneous Catalysis with Single-Atom Alloys. *J. Phys. Chem. Lett.* **2018**, *9*, 5636−5646.

(47) Giannakakis, G.; Flytzani-Stephanopoulos, M.; Sykes, E. C. H. Single-Atom Alloys as a Reductionist Approach to the Rational Design of Heterogeneous Catalysts. *Acc. Chem. Res.* **2019**, *52*, 237−247.

(48) Peng, P.; Li, Y.; Cheng, Y.; Deng, S.; Chen, P.; Ruan, R. Atmospheric Pressure Ammonia Synthesis Using Non-Thermal Plasma-Assisted Catalysis. *Plasma Chem. Plasma Process.* **2016**, *36*, 1201−1210.

(49) Mehta, P.; Barboun, P.; Herrera, F. A.; Kim, J.; Rumbach, P.; Go, D. B.; Hicks, J. C.; Schneider, W. F. Overcoming Ammonia Synthesis Scaling Relations with Plasma-Enabled Catalysis. *Nature Catalysis* **2018**, *1*, 269−275.

(50) Grabow, L.; Xu, Y.; Mavrikakis, M. Lattice Strain Effects on CO Oxidation on Pt(111). *Phys. Chem. Chem. Phys.* **2006**, *8*, 3369−3374.

(51) Wang, L.; Zeng, Z.; Gao, W.; Maxson, T.; Raciti, D.; Giroux, M.; Pan, X.; Wang, C.; Greeley, J. Tunable Intrinsic Strain in Two-Dimensional Transition Metal Electrocatalysts. *Science* **2019**, *363*, 870−874.

(52) Khorshidi, A.; Violet, J.; Hashemi, J.; Peterson, A. A. How Strain Can Break the Scaling Relations of Catalysis. *Nature Catalysis* **2018**, *1*, 263−268.

(53) Liu, F.; Xue, T.; Wu, C.; Yang, S. Coadsorption of CO and O over Strained Metal Surfaces. *Chem. Phys. Lett.* **2019**, *722*, 18−25.

(54) Che, F.; Gray, J. T.; Ha, S.; Kruse, N.; Scott, S. L.; McEwan, J. S. Elucidating the Roles of Electric Fields in Catalysis: A Perspective. *ACS Catal.* **2018**, *8*, 5153−5174.

(55) Kruezer, K. J.; Wang, R. L. C. Physics and Chemistry in High Electric Fields. *Philos. Mag. B* **1994**, *69*, 945−955.

(56) Kreuzer, H. J., Surface Physics and Chemistry in High Electric Fields. In *Chemistry and Physics of Solid Surfaces VIII. Springer Series in Surface Sciences*; Vanselow, R., Howe, R., Eds.; Springer: Berlin, 1990; Vol. 22.

(57) Kim, C. H.; Frisbie, C. D. Field Effect Modulation of Outer-Sphere Electrochemistry at Back-Gated, Ultrathin ZnO Electrodes. *J. Am. Chem. Soc.* **2016**, *138*, 7220−7223.

(58) Wang, Y.; Kim, C. H.; Yoo, Y.; Johns, J. E.; Frisbie, C. D. Field Effect Modulation of Heterogeneous Charge Transfer Kinetics at Back-Gated Two-Dimensional MoS2 Electrodes. *Nano Lett.* **2017**, *17*, 7586−7592.

(59) Pettersson, L. G. M.; Nilsson, A. A Molecular Perspective on the d-Band Model: Synergy Between Experiment and Theory. *Top. Catal.* **2014**, *57*, 2−13.

(60) Hammer, B.; Norskov, J. K. Why Gold is the Noblest of all Metals. *Nature* **1995**, *376*, 238−240.

(61) Nilsson, A.; Pettersson, L. G. M.; Hammer, B.; Bligaard, T.; Christensen, C. H.; Norskov, J. K. The Electronic Structure Effect in Heterogeneous Catalysis. *Catal. Lett.* **2005**, *100*, 111−114.

(62) Wang, L.; Zeng, Z.; Gao, W.; Maxson, T.; Raciti, D.; Giroux, M.; Pan, X.; Wang, C.; Greeley, J. Tunable Intrinsic Strain in Two-Dimensional Transition Metal Electrocatalysts. *Science* **2019**, *363*, 870−874.

(63) Francis, M. F.; Curtin, W. A. Mechanical Stress Combined with Alloying May Allow Continuous Control over Reactivity: Strain Effects on CO Dissociation and Subsequent Methanation Catalysis over Ni(211), Ni3Fe(211), and NiFe(112). *J. Phys. Chem. C* **2017**, *121*, 6113−6119.

(64) Kim, C. H.; Wang, Y.; Frisbie, C. D. Continuous and Reversible Tuning of Electrochemical Reaction Kinetics on Back-Gated 2D Semiconductor Electrodes: Steady-State Analysis Using a Hydrodynamic Method. *Anal. Chem.* **2019**, *91*, 1627−1635.

(65) Imbihl, R. Electrochemical Promotion of Catalytic Reactions. *Prog. Surf. Sci.* **2010**, *85*, 241.

(66) Neophytides, S. G.; Vayenas, C. G. TPD and Cyclic Voltammetric Investigation of the Origin of Electrochemical Promotion in Catalysis. *J. Phys. Chem.* **1995**, *99*, 17063.

(67) Ladas, S.; Kennou, S.; Bebelis, S.; Vayenas, C. G. Origin of Non-Faradaic Electrochemical Modification of Catalytic Activity. *J. Phys. Chem.* **1993**, *97*, 8845.

(68) Basini, L.; Cavalca, C. A.; Haller, G. L. J. Electrochemical Promotion of Oxygen Atom Back-Spillover from Yttria-Stabilized Zirconia onto a Porous Platinum Electrode: Detection of SERS Signals. *J. Phys. Chem.* **1994**, *98*, 10853.

(69) Ladas, S.; Bebelis, S.; Vayenas, C. G. Work Function Measurements on Catalyst Films Subject to in situ Electrochemical Promoation. *Surf. Sci.* **1991**, *251−252*, 1062.

(70) Mhadeshwar, A. B.; Wang, H.; Vlachos, D. G. Thermodynamic Consistency in Microkinetic Development of Surface Reaction Mechanisms. *J. Phys. Chem. B* **2003**, *107* (46), 12721−12733.